ACSNANO

www.acsnano.org

ARTICLE

Circulation Time-Optimized Albumin Nanoplatform for Quantitative Visualization of Lung Metastasis via Targeting of Macrophages

Hyewon Chung,[‡] Ji Yong Park,[‡] Kyuwan Kim, Ran Ji Yoo, Minseok Suh, Gyo Jeong Gu, Jin Sil Kim, Tae Hyeon Choi, Jung Woo Byun, Young Wook Ju, Wonshik Han, Han Suk Ryu, Gehoon Chung, Do Won Hwang, Yujin Kim, Hye-Ryun Kang, Yi Rang Na, Hongyoon Choi, Hyung-Jun Im, Yun-Sang Lee,* and Seung Hyeok Seok*

Cite This: https://doi.org/10.1021/acsnano.2c03075

Read Online

ACCESS | Metrics & More | Article Recommendations | Supporting Information

ABSTRACT: **The development of molecular imaging probes to identify key cellular changes within lung metastases may lead to noninvasive detection of metastatic lesions in the lung. In this study, we constructed a macrophage-targeted clickable albumin nanoplatform (CAN) decorated with mannose as the targeting ligand using a click reaction to maintain the intrinsic properties of albumin *in vivo*. We also modified the number of mannose molecules on the CAN and found that mannosylated serum albumin (MSA) harboring six molecules of mannose displayed favorable pharmacokinetics that allowed high-contrast imaging of the lung, rendering it suitable for *in vivo* visualization of lung metastases. Due to the optimized control of functionalization and surface modification, MSA enhanced blood circulation time and active/passive targeting abilities and was specifically incorporated by mannose receptor (CD206)-expressing macrophages in the metastatic lung. Moreover, extensive *in vivo* imaging studies using single-photon emission computed tomography (SPECT)/CT and positron emission tomography (PET) revealed that blood circulation of time-optimized MSA can be used to discern metastatic lesions, with a strong correlation between its signal and metastatic burden in the lung.**

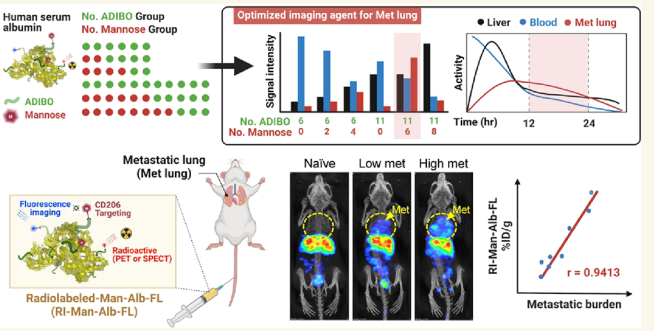

KEYWORDS: *lung metastasis, albumin nanoplatform, macrophage, noninvasive imaging, blood circulation*

INTRODUCTION

The lung is a frequent site of metastases from various cancers, including breast, skin, and colon cancer, and lung metastases in patients correlate with unfavorable prognosis.[1] Thus, early detection of lung metastasis can be beneficial for patients, as it will enable administration of appropriate and timely therapeutic interventions.

To detect metastatic lesions, positron emission tomography (PET), computed tomography (CT), and/or magnetic resonance imaging (MRI) are currently being used as standard noninvasive strategies.[2−4] However, their sensitivity in detecting small metastases is limited.[5,6] Several types of nanoplatforms have been developed to overcome this limitation; however, the pharmacokinetic limitations of the existing nanoplatforms in reaching the metastatic lung constitute a major hurdle in *in vivo* imaging of lung metastases.[7−10] For example, suboptimal blood circulation time and rapid clearance by the reticuloendothelial system (RES), including the liver, compromise the retention and transportation of nanoplatforms to the lungs. Furthermore, the functionalization of nanoplatforms to enhance specific targeting may alter their intrinsic properties and *in vivo* biodistribution, rendering them unsuitable for detecting the metastatic lung, particularly poorly vascularized and small

Received: March 29, 2022
Accepted: August 1, 2022

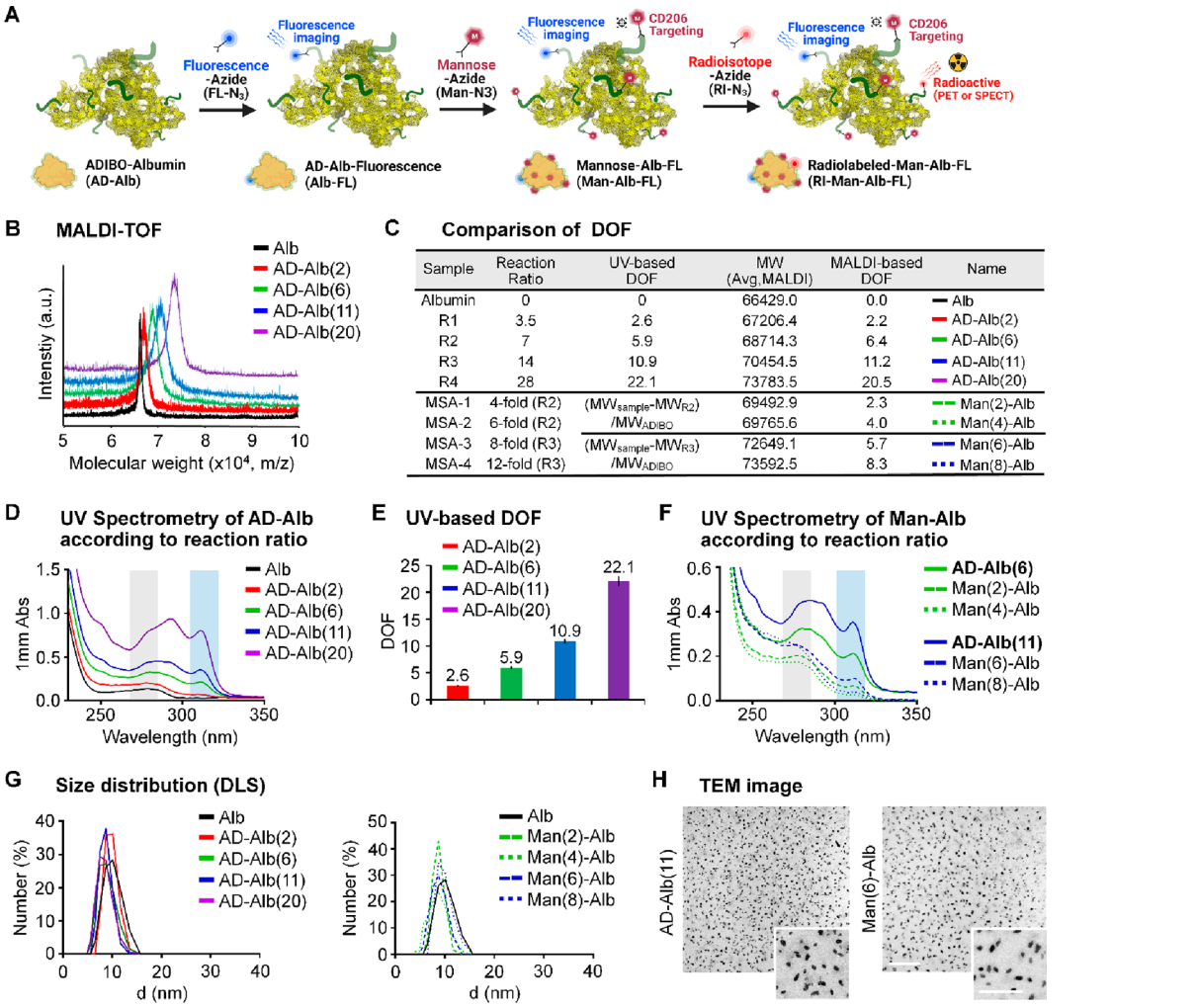

Sample	Reaction Ratio	UV-based DOF	MW (Avg.MALDI)	MALDI-based DOF	Name
Albumin	0	0	66429.0	0.0	Alb
R1	3.5	2.6	67206.4	2.2	AD-Alb(2)
R2	7	5.9	68714.3	6.4	AD-Alb(6)
R3	14	10.9	70454.5	11.2	AD-Alb(11)
R4	28	22.1	73783.5	20.5	AD-Alb(20)
MSA-1	4-fold (R2)	$(MW_{sample}-MW_{R2})$	69492.9	2.3	Man(2)-Alb
MSA-2	6-fold (R2)	$/MW_{ADIBO}$	69765.6	4.0	Man(4)-Alb
MSA-3	8-fold (R3)	$(MW_{sample}-MW_{R3})$	72649.1	5.7	Man(6)-Alb
MSA-4	12-fold (R3)	$/MW_{ADIBO}$	73592.5	8.3	Man(8)-Alb

Figure 1. Construction and characterization of MSA. (A) Schematic representation of MSAs using click reaction in AD-Alb with other functional molecules. (B) MALDI-TOF data of AD-Alb according to the reaction ratio. (C) Comparison of DOF on each albumin sample using UV-based analysis and MALDI-TOF-based calculation. (D) UV spectrum of the same albumin sample used in MALDI-TOF measurement of AD-Albs. (E) UV-based calculated data of each type of AD-Albs. (F) UV-spectrum of Man-Alb and AD-Alb according to reaction ratio. (G) Size data of all AD-Alb and Man-Alb using DLS after averaging five measurements. (H) TEM image analysis using selected samples to be used for *in vitro* and *in vivo* experiments. Scale bar = 500 nm; 250 nm for the magnified images.

metastatic lesions. Thus, a strategy that utilizes both passive and active targeting and enhances retention time and specific cellular internalization within metastatic lesions is required.

The use of macrophages is potentially beneficial for *in vivo* imaging of lung metastases. Macrophages are preferentially recruited to metastatic microenvironments,[11,12] in which they avidly incorporate nanoparticles via phagocytosis or endocytosis, favoring the accumulation of injected nanoparticles at metastatic sites without functionalization. Moreover, macrophages exhibit high tissue-penetrating ability into the poorly vascularized hypoxic regions within the tumor.[13−16] Thus, taking advantage of the aforementioned characteristics of macrophages, nanoparticles functionalized with ligands specific for metastasis-associated macrophages would further improve the targeting efficiency of the nanoformulations and enable sensitive detection of lung metastasis. We have previously used mannose as a target ligand for active targeting of macrophages that highly express the mannose receptor.[17,18] So far, several nanomaterials, including iron oxide, polymers, and liposomes, have been introduced as potential candidates for CD206-targeted *in vivo* imaging.[19−24] However, imaging using these nanomaterials in the clinic may be challenging because of their large size, immunogenicity, and regulatory hurdles associated with modification. Furthermore, current imaging strategies that target CD206-expressing macrophages are primarily aimed at imaging primary tumors or draining lymph nodes,[25,26] whereas distant metastases including those to the lung, other than the lymph node, have not been considered completely in previous studies.

Human serum albumin (HSA) has emerged as a promising biomolecule, as it is biologically compatible and can be easily modified using surface chemistry for drug delivery carriers.[27,28] In addition, the long circulation half-life of HSA enhances the efficacy of drug delivery to the target site via enhanced permeability and retention (EPR) effects.[29] Thus, compared to other nanomaterials, the small size, low immunogenicity, and excellent biocompatibility of HSA render it advantageous for *in vivo* diagnostic imaging and targeted delivery. Interestingly, a recent study using an albumin-based platform for *in vivo* imaging of CD206-expressing macrophages showed promising results in tumor imaging; however, metastatic lesions were not diagnosed satisfactorily.[26] One possible reason for this failure is

https://doi.org/10.1021/acsnano.2c03075
ACS Nano XXXX, XXX, XXX−XXX

that albumin formed clusters with an average size of 130−140 nm, which is ∼16-fold larger than the conventional size of albumin (6−8 nm).[26,30] As the properties of albumin may be altered during functionalization depending on the conditions and compounds used in the reaction, harsh conditions such as low or high pH or using reducing agents presumably led to albumin aggregation, thereby shortening the *in vivo* circulation half-life and limiting its accumulation at metastatic sites, including the lungs, as confirmed by similar levels of uptake of CD206-targeted and nontargeted HSA.

To circumvent these problems, we recently reported a click chemistry-based nanoplatform in which a clickable albumin nanoplatform (CAN) was easily functionalized for *in vivo* imaging with sufficient circulation half-life.[31] Moreover, as the physical and radiochemical properties of albumin were maintained to some extent during functionalization, the potency of HSA *in vivo* may be further amplified by the EPR effect, as well as the secreted protein acidic and rich in cysteine (SPARC) produced in the local metastatic microenvironment,[32] thereby facilitating cellular internalization of HSA within the metastatic sites.

Here, we report the design, synthesis, and optimization of mannosylated serum albumin (MSA) as an imaging probe for detecting metastatic lung lesions. The optimized MSA was preferentially internalized by metastasis-associated macrophages, and thus, lung metastatic lesions were quantitatively visualized in tumor models. Hence, we believe that noninvasive imaging of MSA may be a promising strategy for the identification of lung metastatic lesions, which may increase the therapeutic output in a substantial number of patients.

RESULTS AND DISCUSSION

Construction and Characterization of MSA. Based on previously reported half-life data,[31] we selected the degree of functionalization (DOF) of CAN and functionalized it using Man-N_3 as a targeting molecule to synthesize MSA (Figures 1A and S1A), while the range of modification level was selected using slightly different reaction ratios. In addition, as the mannose level is known to affect targeting ability, click reaction conditions in which the number of mannose molecules on the albumin surface differed by two conjugation levels each were used.[33] Reactions 1 (R1) to 4 (R4) had molar ratios of albumin to azadibenzocyclooctyne-*N*-hydroxysuccinimide (ADIBO-NHS) of 3.5, 7, 14, and 28, respectively. Matrix-assisted laser desorption ionization time-of-flight (MALDI-TOF) spectroscopy showed that the mass increased according to the reaction ratio (Figure 1B). The increase in molecular weight according to reaction ratios and the number of attached ADIBOs and DOFs can be calculated, as confirmed using MALDI-TOF bases DOF (Figure 1C). The UV−visible spectrum also showed increase in peak intensities at specific wavelengths for both albumin (peak intensity at 280 nm, black square box) and ADIBO (peak intensity at 309 nm, blue square box) according to the reaction ratio (Figure 1D). The methods for calculating DOF were confirmed previously using a simple equation that shows the correlation between the MALDI-TOF results and intraclass correlation (ICC) of 0.991 (Figure S1B).[31] The peak intensities of albumin and ADIBO showed correlation coefficient (R^2) of 0.9992, indicating that the increase in peak intensity at the wavelength of albumin was due to the change in peak intensity of ADIBO. The UV-based number of attached ADIBOs and DOFs can be calculated and shown in UV-based DOF bases (Figure 1C and E). We prepared CANs with different DOFs and finally chose R2 and R3 as candidates for further experiments. The CAN with six DOFs was denoted as AD-Alb(6), which was synthesized using the R2 reaction conditions. Eleven DOFs were denoted as AD-Alb(11) and were synthesized under R3 reaction conditions. For *in vitro* fluorescence imaging, both AD-Alb(6) and AD-Alb(11) were conjugated to an azide functional dye (FL-N_3). To optimize the number of mannose molecules on Albs, we added azide functional mannose (Man-N_3) to AD-Alb(6) and AD-Alb(11) at different reaction ratios (4-, 6-, 8-, and 12-fold excesses). Finally, we prepared mannose-functionalized HSAs with four different mannose levels, with two, four, six, and eight DOFs, denoted as Man(2)-Alb-FL, Man(4)-Alb-FL, Man(6)-Alb-FL and Man(8)-Alb-FL, respectively. In addition, Man(6)-Alb-FL, described later, has the same number of FLs as Alb(11)-FL. Subsequently, even if FL is not mentioned, same quantities of it are always conjugated to all CANs. The UV and MALDI-based data and calculated results are shown using the same methods of CAN formulation (Figures 1C,F and S2A).

Further analysis was performed to measure the molecular sizes and zeta potentials (Figure 1G and Table 1) of AD-Alb and Man-Alb using dynamic light scattering (DLS). The hydrodynamic diameters of all products were similar irrespective of the DOF and mannose levels. The sizes and size distributions of all Man-Alb, including AD-Alb, used as imaging agents for the animal model, were also measured using the DLS method and were found to be almost similar (8−9 nm) to that of natural albumin (Figure S2B), and the polydispersity index (PDI) values were around 0.2, except those of AD-Alb(20), which were slightly high, but had no considerable effect on *in vivo* imaging for targeting macrophages. However, the zeta potentials tended to decrease as the DOFs increased, which represents the masking of the amine group on albumin (Table 1). The MSAs also showed slightly different zeta values; however, the results were within the margin of error. The morphologies of AD-Alb(11) and Man(6)-Alb were examined using transmission electron microscopy (TEM). As shown in the TEM images, AD-Alb(11) and Man(6)-Alb exhibited a uniform morphology, with an average size of ∼10 nm (Figure 1H). The structures of other AD-Alb and MSAs were also confirmed by TEM (Figure S3). It is noteworthy that, unlike conventional albumin nanoclusters, MSAs maintained their original size and morphology even after various modifications, including conjugation with ADIBO-NHS, click reactions with mannose, and fluorescence dyes.

Table 1. Size and Zeta Potential of Samples

sample	size (nm)	PDI	zeta potential (mV)
albumin	9.844 ± 1.8	0.217	−14.1 ± 4.44
AD-Alb(2)	9.568 ± 1.3	0.233	−16.7 ± 9.36
AD-Alb(6)	8.604 ± 1.6	0.211	−18.1 ± 10.5
AD-Alb(11)	8.503 ± 1.2	0.276	−20.6 ± 4.24
AD-Alb(20)	8.246 ± 1.5	0.405	−34.7 ± 7.27
Man(2)-Alb	8.539 ± 0.7	0.241	−20.7 ± 8.81
Man(4)-Alb	8.882 ± 0.4	0.210	−21.8 ± 13.4
Man(6)-Alb	8.544 ± 0.6	0.211	−22.1 ± 7.30
Man(8)-Alb	8.578 ± 0.4	0.226	−23.4 ± 5.51

Pharmacokinetics and Biodistribution of MSA. DOF alters the pharmacokinetics and *in vivo* distribution of albumin. As DOF increased, circulation time and blood pool activity

https://doi.org/10.1021/acsnano.2c03075
ACS Nano XXXX, XXX, XXX−XXX

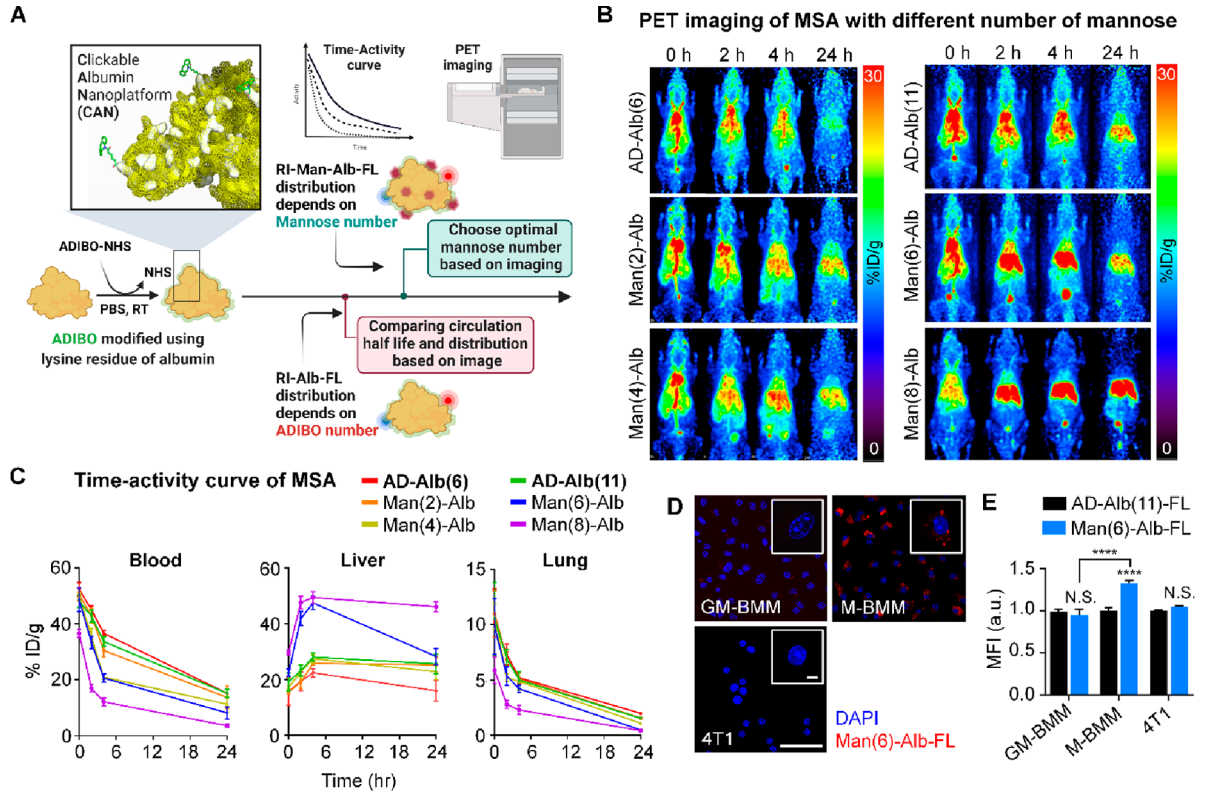

Figure 2. Pharmacokinetics and biodistribution of MSA. (A) Image-based evaluation strategy according to the number of ADIBO groups and mannose for optimized image agent. (B) Alteration of biodistribution according to DOF. The biodistribution of AD-Alb(6) and AD-Alb(11) was compared using serial *in vivo* PET imaging as a control for selecting the optimal number of Man-Albs. (C) Time−activity curve of AD-Albs and Man-Albs in the blood, liver, and lung. The graph shows the *in vivo* pharmacokinetics of the imaging agent. n = 5 mice/group. (D) Representative confocal immunofluorescent images of Man(6)-Alb-FL (red) and DAPI (nucleus, blue) in GM-BMM, M-BMM, and 4T1 cells. Scale bar = 50 μm. (E) Quantification of *in vitro* uptake of AD-Alb(11)-FL or Man(6)-Alb-FL as measured using flow cytometry after incubation for 1 h. n = 4−6/group. Data are normalized to each cell (GM-BMM, M-BMM, and 4T1) treated with AD-Alb(11)-FL. Data show means ± SEM. ****P < 0.0001 using Student's t test. N.S.: nonsignificant.

tended to decrease, whereas liver uptake significantly increased. In this context, low DOF may be more advantageous than high DOF; however, the number of functional groups of low DOF that can be added is limited. In addition, imaging probes with blood retention can show stronger signals in the lungs, which renders differentiation of small metastatic lesions in the lungs challenging. To address this issue, we performed biodistribution studies of MSA derivatives with different conjugation levels of mannose using PET imaging analysis to determine the optimal pharmacokinetic properties of MSAs as *in vivo* lung imaging agents in healthy mice (Figure 2A). We introduced two or four mannose molecules into AD-Alb(6) and six or eight mannose molecules into AD-Alb(11) and compared their biodistribution based on the images (Figure 2B). As expected, AD-Alb(6) and AD-Alb(11) showed a similar distribution pattern and circulation half-life of 6.75 ± 0.85 and 6.98 ± 1.80 h, respectively (Figure 2C and Table 2). Interestingly, despite the same DOF, the blood circulation half-life differed significantly with the mannose level (Tables 2 and 3). As the amount of mannose increased, higher liver uptake was observed 2 h after injection (Table 3). In the case of two or four mannose residues, liver uptake increased with time compared to that observed for AD-Alb(6), although the difference in imaging was not sufficient for it to qualify as an imaging probe. However, for Man(6)-Alb, which has six mannose residues, the blood circulation half-life was as high as that of Man(4)-Alb, while it showed high liver uptake, similar

Table 2. Pharmacokinetics of MSAs with Different DOFs

	$T_{1/2\alpha}$ (h)		$T_{1/2\beta}$ (h)	
	avg	SD	avg	SD
AD-Alb(6)	6.75	0.85	19.08	0.92
AD-Alb(11)	6.98	1.80	21.05	5.21
Man(2)-Alb	5.19	0.95	24.84	6.73
Man(4)-Alb	3.44	0.14	20.24	1.11
Man(6)-Alb	3.49	0.17	19.21	4.05
Man(8)-Alb	2.99	0.12	16.48	1.65

to that observed for Man(8)-Alb. In particular, Man(6)-Alb and Man(8)-Alb showed a low image signal of the lungs after 24 h; therefore, it was possible to select an imaging time point to monitor metastatic lesions in the lung. In addition, the elimination time (β half-life, $T_{1/2\beta}$) indicated the removal time from the blood, which tended to decrease with increase in mannose level (Table 2). In particular, Man(6)-Alb had similar $T_{1/2\beta}$ values as those of AD-Albs, and liver uptake was as high as that of Man(8)-Alb; hence, it is considered to be the most optimized MSA for *in vivo* lung imaging. At this time, as the β half-life of Man(6)-Alb is almost 19 h, we concluded that obtaining images after that time point can minimize the effect of signals from the blood pool. Importantly, at 24 h, Man(6)-Alb imaging showed similar levels of liver uptake as AD-Alb(11). In this case, other distribution images of the body at 24 h were similar, whereas only the metastatic lung might

https://doi.org/10.1021/acsnano.2c03075
ACS Nano XXXX, XXX, XXX−XXX

Table 3. Quantification of MSAs Uptake in the Blood, Liver, and Lung with Different DOF of ADIBO and Mannose Group Measured Using PET Imaging

		blood pool (% ID/g)	liver (% ID/g)	lung (% ID/g)
AD-Alb(6)	0 h	52.39 ± 2.46	15.77 ± 4.90	10.25 ± 2.99
	2 h	45.03 ± 1.39	19.40 ± 3.32	7.33 ± 0.97
	4 h	36.64 ± 0.98	22.45 ± 1.50	5.21 ± 0.53
	24 h	15.17 ± 1.56	16.00 ± 3.70	1.98 ± 0.08
Man(2)-Alb	0 h	50.48 ± 2.30	15.48 ± 0.72	11.01 ± 2.1
	2 h	42.97 ± 2.67	19.18 ± 2.33	6.88 ± 0.69
	4 h	30.47 ± 2.25	25.84 ± 0.67	5.11 ± 0.51
	24 h	13.47 ± 4.03	25.30 ± 2.62	1.57 ± 0.05
Man(4)-Alb	0 h	50.22 ± 1.15	17.20 ± 0.56	10.8 ± 1.15
	2 h	35.43 ± 2.81	22.87 ± 2.47	5.22 ± 0.35
	4 h	20.93 ± 0.91	27.50 ± 1.57	4.87 ± 0.81
	24 h	11.27 ± 2.87	22.83 ± 2.73	1.1 ± 0.08
AD-Alb(11)	0 h	48.13 ± 2.19	19.23 ± 3.18	10.53 ± 3.33
	2 h	42.79 ± 2.24	23.23 ± 2.08	6.97 ± 0.78
	4 h	33.67 ± 1.82	28.07 ± 1.46	5.01 ± 0.74
	24 h	15.17 ± 1.56	25.67 ± 3.48	1.54 ± 0.1
Man(6)-Alb	0 h	48.64 ± 4.27	22.50 ± 1.30	9.84 ± 2.54
	2 h	33.33 ± 2.25	41.87 ± 2.51	5.37 ± 0.85
	4 h	20.63 ± 1.53	47.49 ± 2.36	4.22 ± 0.33
	24 h	8.17 ± 2.20	28.27 ± 2.91	0.49 ± 0.04
Man(8)-Alb	0 h	36.59 ± 1.39	29.63 ± 0.80	5.89 ± 1.22
	2 h	17.00 ± 1.35	47.67 ± 2.30	2.8 ± 0.35
	4 h	12.13 ± 1.40	49.43 ± 2.05	2.3 ± 0.4
	24 h	3.63 ± 0.60	46.13 ± 1.83	0.43 ± 0.02

represent different uptake patterns, which depended on mannose targeting to macrophages.

The labeling conditions and efficiency of isotope-labeled AD-Albs and Man-Albs were also determined to assess the feasibility of using them as probes for nuclear medicine imaging (Figure S4). In particular, as it is postlabeling via a click reaction, the effects on physiochemical and morphology could be minimized, and the stability of the label was confirmed to ensure its stability as an imaging probe (Figure S5). These results suggested that the optimal number of mannose molecules for obtaining clear and quantitative images of the lung metastasis region using imaging probes is six on AD-Alb(11). Thus, we used Man(6)-Alb as an *in vivo* circulation-controlled imaging probe in subsequent analyses.

We next examined the cellular uptake of Man(6)-Alb. *In vitro* uptake of Man(6)-Alb was confirmed by the fact that Man(6)-Alb uptake was more evident in M-CSF-grown bone marrow-derived macrophages (M-BMMs), which expresses higher levels of CD206, than in GM-CSF-grown bone marrow-derived macrophages (GM-BMMs) and 4T1 (Figures 2D,E and S6A). Additionally, we tested the cytotoxicity and specificity of Man(6)-Alb uptake in M-BMMs. The incubation of M-BMMs with Man(6)-Alb for 24 h showed little cytotoxicity (Figure S6B), and pretreatment of a saturating amount of mannan (a natural ligand for CD206) effectively blocked the binding to CD206, thereby leading to a significant inhibition of Man(6)-Alb uptake by M-BMMs (Figure S6C). To further evaluate the specificity of Man(6)-Alb, an *in vivo* blocking study was performed in control mice (tumor-free, TF), and we found that blocking of CD206 using mannan resulted in a marked reduction in liver uptake of Man(6)-Alb to the level comparable to that of untargeted AD-Alb(11) (Figure S7). These findings demonstrated that the internalization of Man(6)-Alb is a CD206-dependent process.

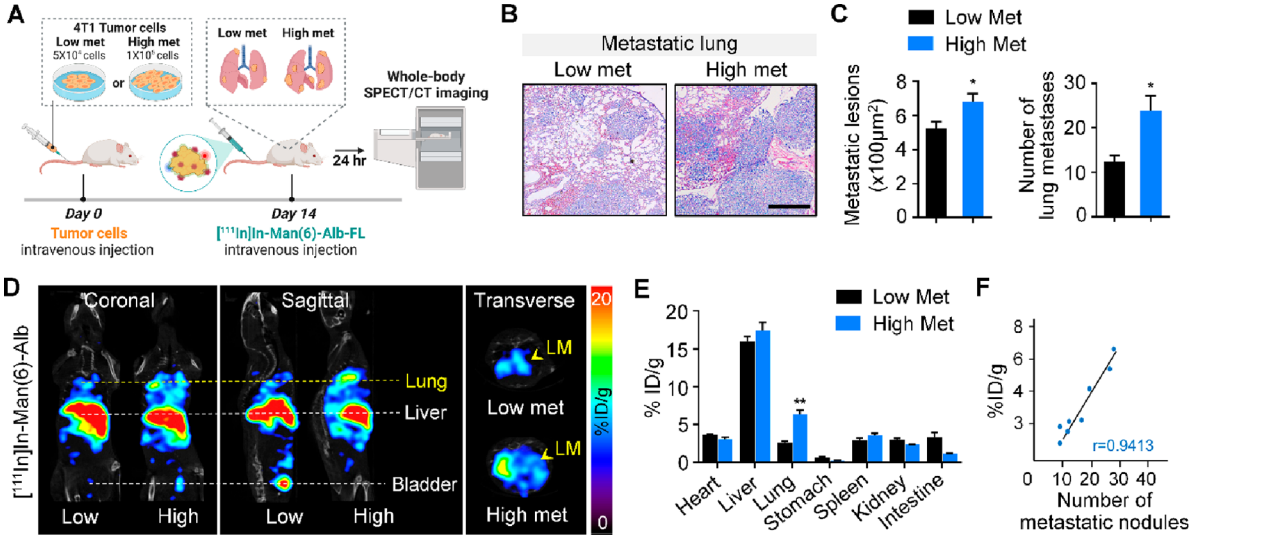

Figure 3. Increase in [^{111}In]In-Man(6)-Alb-FL signal directly correlates with the metastatic burden in the lung. (A) Schematic showing SPECT/CT imaging of lung metastases in mice after intravenous injection of different numbers of 4T1 cancer cells (low met vs high met). (B,C) Different metastatic burdens induced by intravenous injection of low (5×10^4) or high (1×10^5) number of 4T1 cells were confirmed using H&E staining (B) and determining the lesion area of lung metastatic foci and number of lung metastases (C) 14 days after tumor injection. Scale bar = 100 μm. (D) Representative SPECT/CT images (coronal, sagittal, and transverse views) of mice with lower metastases and higher metastases 24 h after [^{111}In]In-Man(6)-Alb-FL injection. [^{111}In]In-Man(6)-Alb-FL was able to detect lung metastases (LM) with significantly higher signal in lungs from the high met group than in those from the low met group. (E) *Ex vivo* biodistribution of [^{111}In]In-Man(6)-Alb-FL in various organs of mice with lung metastases, expressed as % ID/g. (F) Correlation between [^{111}In]In-Man(6)-Alb-FL signal and metastatic burden, as determined by the number of metastatic foci in lungs from 4T1-bearing mice after intravenous tumor injection. n = 3−4 mice/group. Data represent the mean ± SEM. *P < 0.05, **P < 0.01 using Student's t test.

https://doi.org/10.1021/acsnano.2c03075
ACS Nano XXXX, XXX, XXX−XXX

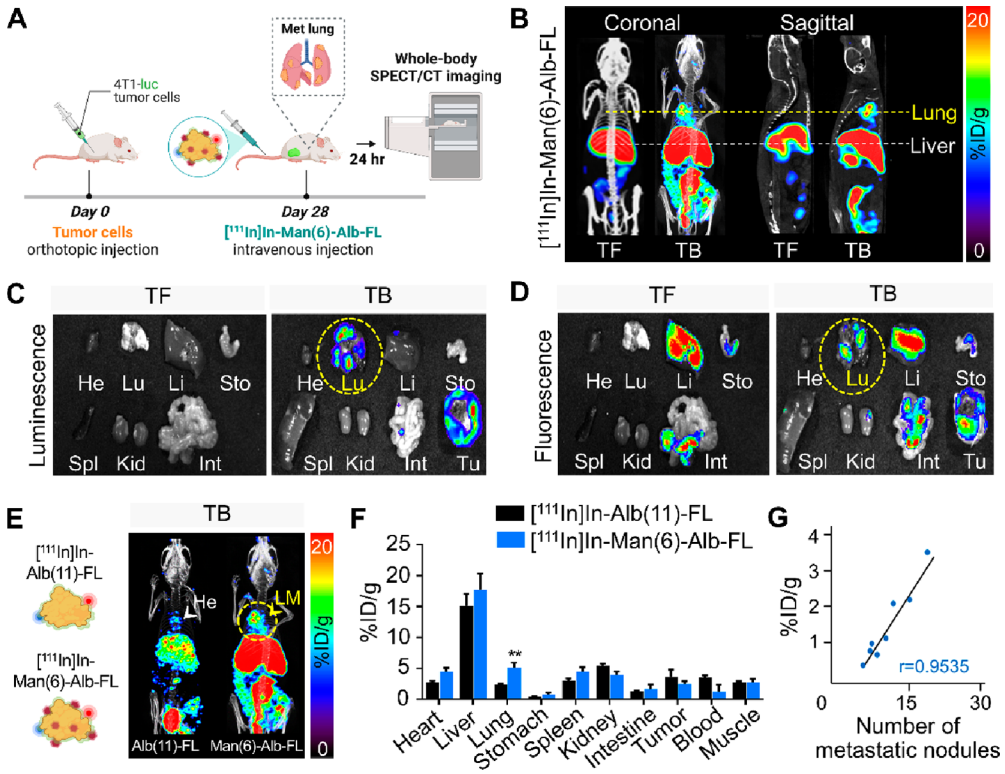

Figure 4. ***In vivo*** **imaging of lung metastases in orthotopic mouse breast tumors. (A) Illustration of orthotopic injection of 4T1-luciferase cells, followed by the intravenous injection of [^{111}In]In-Man(6)-Alb-FL and SPECT/CT imaging. (B) Tumor-free mice (TF, control) and 4T1-bearing mice (TB, day 28) were injected with [^{111}In]In-Man(6)-Alb-FL, and SPECT/CT images were acquired 24 h postinjection. Representative SPECT/CT images (coronal and sagittal views) imaged with [^{111}In]In-Man(6)-Alb-FL revealed strong signals in the lung metastases (day 28). (C,D) Representative luminescence (C) and fluorescence (D) images of multiple dissected organs (heart, lung, liver, stomach, spleen, kidney intestine, and tumor) from tumor-free (TF) and 4T1-bearing mice (TB) after SPECT/CT imaging on day 28. (E) SPECT/CT images of 4T1-bearing mice (TB) injected with [^{111}In]In-Alb(11)-FL or [^{111}In]In-Man(6)-Alb-FL on day 28. While [^{111}In]In-Man(6)-Alb-FL signals were detected in the lungs (LM), [^{111}In]In-Alb(11)-FL signals were only detected in the heart (He), but not in the lungs. (F) *Ex vivo* biodistribution of [^{111}In]In-Alb(11)-FL and [^{111}In]In-Man(6)-Alb-FL in various organs of mice with lung metastases, expressed as % ID/g. (G) Correlation between [^{111}In]In-Man(6)-Alb-FL signal and metastatic burden, as determined from the number of metastatic foci in lungs from 4T1-bearing mice after orthotopic tumor injection. n = 4 mice/group. Data represent the mean ± SD **P < 0.01 using Student's t test.**

Increase in Man(6)-Alb-FL Signal Directly Correlates with the Metastatic Burden in the Lungs. First, we investigated the correlation between [^{111}In]In-Man(6)-Alb-FL uptake and the metastatic burden *in vivo*. Toward this, we constructed an experimental metastasis model, in which 4T1 cancer cells were directly injected into the tail. The degree of metastasis varied with the number of cancer cells injected, i.e., high (1×10^5) or low (5×10^4). Tumor-bearing mice were injected with [^{111}In]In-Man(6)-Alb-FL and imaged after 24 h using SPECT/CT (Figure 3A). The difference in gross metastases in the lungs in these experimental metastasis models was confirmed using histology (Figure 3B and C). As shown in Figure 3D and E, the [^{111}In]In-Man(6)-Alb-FL signal appeared in the metastatic lung after injection and the intensity of the SPECT signal was significantly high in the lungs of mice injected with higher number of cancer cells (high met) than in those injected with lower number (low met). The CD206-targeting specificity was further confirmed by a decreased signal in metastatic lung after injection of [^{111}In]In-Man(6)-Alb-FL with a blocking dose of mannan (Figure S8). Interestingly, [^{111}In]In-Man(6)-Alb-FL showed excellent linear correlation (r = 0.9413) between the signal intensity and metastatic burden, as is evident from the number of metastatic nodules in the lung after intravenous injection of cancer cells (Figure 3F). The capability of [^{111}In]In-Man(6)-Alb-FL for the noninvasive detection of metastatic lesions was further tested in a metastatic B16F10 melanoma model (Figure S9). Collectively, our data suggested that MSA is a clinically applicable tracer with superior sensitivity and specificity that is sufficient to noninvasively discern metastatic lesions with strong correlation with the metastatic burden.

In Vivo **Imaging of Lung Metastases in Orthotopic Mouse Breast Tumors.** The targeting ability and specificity of Man(6)-Alb-FL for the detection of spontaneous lung metastases *in vivo* were evaluated in 4T1 tumor-bearing mice. Twenty-8 days after inoculating the orthotopic luciferase-expressing 4T1 (4T1-luc), control mice (TF) and tumor-bearing mice (TB) with lung metastases were intravenously injected with [^{111}In]In-Man(6)-Alb-FL, and SPECT/CT images were acquired 24 h postinjection (Figure 4A). In addition to the substantial uptake by the tumors, we demonstrated clearly high uptake in the lungs of 4T1-bearing mice (TB), whereas no signal was observed in the lungs of control mice (TF) (Figure 4B). Major organs, including the heart, lung, liver, stomach, spleen, kidney, and intestine, and the tumor, were excised immediately after imaging and subjected to *ex vivo* imaging of colabeled FNR648 fluorescence. In agreement with the results of whole body

https://doi.org/10.1021/acsnano.2c03075
ACS Nano XXXX, XXX, XXX−XXX

imaging, *ex vivo* fluorescence imaging confirmed that [^{111}In]In-Man(6)-Alb-FL was incorporated by the lungs of tumor-bearing mice, in which metastasis was confirmed using bioluminescence imaging of injected 4T1-luc cells (Figures 4C and D). The uptake of [^{111}In]In-Man(6)-Alb-FL by the liver was also observed in both tumor-free and tumor-bearing mice, mainly because of the presence of CD206-expressing Kupffer cells in this organ. [^{111}In]In-Man(6)-Alb-FL was also found to be excreted via hepatobiliary routes, as indicated by the deposition of fluorescence in the gastrointestinal tract (Figure 4D).

To further demonstrate the specificity of MSA for *in vivo* applications, we directly compared [^{111}In]In-Man(6)-Alb-FL with nontargeted albumin [^{111}In]In-Alb(11)-FL. First, in tumor-free mice, the biodistribution was checked 24 h postinjection of [^{111}In]In-Alb(11)-FL and [^{111}In]In-Man(6)-Alb-FL. The lung uptake was similarly measured (Figure S10). Interestingly, in tumor-bearing mice, [^{111}In]In-Man(6)-Alb-FL uptake in the metastatic lung was significantly higher than that of [^{111}In]In-Alb(11)-FL, which was also confirmed using the biodistribution analysis of [^{111}In]In-Alb(11)-FL and [^{111}In]In-Man(6)-Alb-FL (Figures 4E,F and Table 4). A linear correlation was also observed between the [^{111}In]In-Man(6)-Alb-FL signals in the lung (% ID/g) and metastatic burden, as determined from the number of metastatic nodules in the lung (r = 0.9535, Figure 4G). Taken together, these data showed that the high accumulation of [^{111}In]In-Man(6)-Alb-FL in the metastatic lung was attributed to the CD206-specific binding affinity of Man(6)-Alb-FL during functionalization and its long circulation time *in vivo*.

Table 4. Quantification of Uptake of [^{111}In]In-Alb(11)-FL or [^{111}In]In-Man(6)-Alb-FL in the Blood, Liver, and Lung from 4T1 Tumor-Bearing Mice Measured Using PET Imaging

	blood pool (% ID/g)	liver (% ID/g)	lung (% ID/g)
[^{111}In]In-Alb(11)-FL	3.62 ± 0.28	15.13 ± 1.91	2.41 ± 0.15
[^{111}In]In-Man(6)-Alb-FL	1.28 ± 1.1	17.73 ± 2.56	5.11 ± 0.82

Confirmation of Man(6)-Alb-FL as a Macrophage-Targeted Probe. To monitor the selective targeting of [^{111}In]In-Man(6)-Alb-FL among cells within the metastatic organ, the lungs were collected immediately after imaging, followed by sectioning and staining with CD206. CD206-expressing macrophages were predominantly localized adjacent to metastatic lesions in the lungs, and the niches where macrophages accumulated showed [^{111}In]In-Man(6)-Alb-FL fluorescence (Figure 5A). Confocal imaging at higher magnification allowed direct visualization of [^{111}In]In-Man(6)-Alb-FL uptake by macrophages at the cellular level (Figure 5B). For further evaluation, we quantitatively analyzed uptake using flow cytometry. [^{111}In]In-Man(6)-Alb-FL uptake by CD206$^+$ macrophages was approximately 4 times higher than that by CD206$^-$ macrophages (Figure 5C).

Interestingly, comparison of the signal intensity of [^{111}In]In-Man(6)-Alb-FL and [^{111}In]In-Alb(11)-FL in CD206$^+$ macrophages from 4T1-bearing mice revealed a significantly higher signal of [^{111}In]In-Man(6)-Alb-FL than that of [^{111}In]In-Alb(11)-FL (Figure 5D), providing additional evidence that active targeting with [^{111}In]In-Man(6)-Alb-FL leads to preferential accumulation in metastasis-associated macrophages, which was beyond the mere passive uptake of albumin via the EPR effect. Similarly, SPECT imaging revealed sufficient accumulation of [^{111}In]In-Man(6)-Alb-FL in the tumor 3−72 h after injection (Figure S11A) and confirmed its CD206-specific uptake (Figure S11B−D).

Multimodal Imaging of Man(6)-Alb-FL in Lung Metastasis Models. Based on the ability of Man(6)-Alb-FL to visualize lung metastasis with low metastatic burden as well as the strong correlation between its signal and metastatic burden in experimental metastasis models (Figure 3), we further applied MSA to monitor small metastatic lesions in the spontaneous metastasis model. In the established models, the 4T1 cancer cells allowed colonization to result in the formation of discrete metastatic lesions on day 21, as confirmed using histological analyses, which grew to overt metastases in the lung on day 28 after the orthotopic injection of the cancer cells. To monitor the signal in the lungs of the 4T1-bearing mice on days 21 and 28 with different degrees of metastatic burden, we injected [^{111}In]In-Man(6)-Alb-FL and found that the signal intensity gradually increased in the lungs until day 28 when substantial metastatic nodules were observed (Figure 6A). [^{111}In]In-Man(6)-Alb-FL also showed lymph node metastases on day 28. Most notably, [^{111}In]In-Man(6)-Alb-FL imaging showed distinct signals in the lungs on day 21, as evidenced by image-based visual analysis and a 5.6-fold increase in the [^{111}In]In-Man(6)-Alb-FL signal (% ID/g) compared to that in the tumor-free mice (Figure 6B). Furthermore, *ex vivo* biodistribution was similar in most of organs, except for that in the lung with low metastases, which showed a higher uptake of [^{111}In]In-Man(6)-Alb-FL (Figure 6C).

We next investigated whether MSA could be a feasible PET imaging probe, which is the preferred choice in relevant clinical fields. We performed [^{64}Cu]Cu-Man(6)-Alb-FL PET/MRI imaging using the same approach as that used for [^{111}In]In-Man(6)-Alb-FL to detect lung metastases in two different syngeneic models of metastasis (4T1- and Lewis lung carcinoma [LLC]-bearing mice). [^{64}Cu]Cu-Man(6)-Alb-FL was successfully applied to monitor metastatic progression in the lungs of 4T1 and LLC tumor-bearing mice (Figures 6D and S12A,B). In addition, PET imaging of 4T1-bearing mice after injection of [^{64}Cu]Cu-Man(6)-Alb-FL with and without a blocking dose of mannan showed high and specific accumulation of [^{64}Cu]Cu-Man(6)-Alb-FL in the lung when only a few microsized metastatic lesions were visible on day 21 (Figures 6E and S13), as confirmed using hematoxylin and eosin (H&E) staining of the excised lung after *in vivo* imaging (Figure 6F). However, metastatic lesions were not clearly discernible using MRI and CT imaging in the same mice (Figures 6G,H and S12C).

Collectively, these data demonstrated that MSA imaging, along with clinically applicable imaging modalities (either SPECT/CT or PET/MRI), enables the early diagnosis of lung metastasis with noninvasive evaluation of the degree of metastatic burden.

Fluorescence Imaging of Human Breast Cancer Tissues with Man(6)-Alb-FL. To validate the clinical applicability of Man(6)-Alb-FL for diagnostic imaging, CD206 expression was evaluated in estrogen receptor (ER)$^+$/progesterone receptor (PR)$^+$ and malignant triple-negative (TN) breast cancer tissues. We found that CD206 expression in TN tissues was substantially higher than that in ER$^+$/PR$^+$ tissues (Figure S14A and B). In addition, CD206

https://doi.org/10.1021/acsnano.2c03075
ACS Nano XXXX, XXX, XXX−XXX

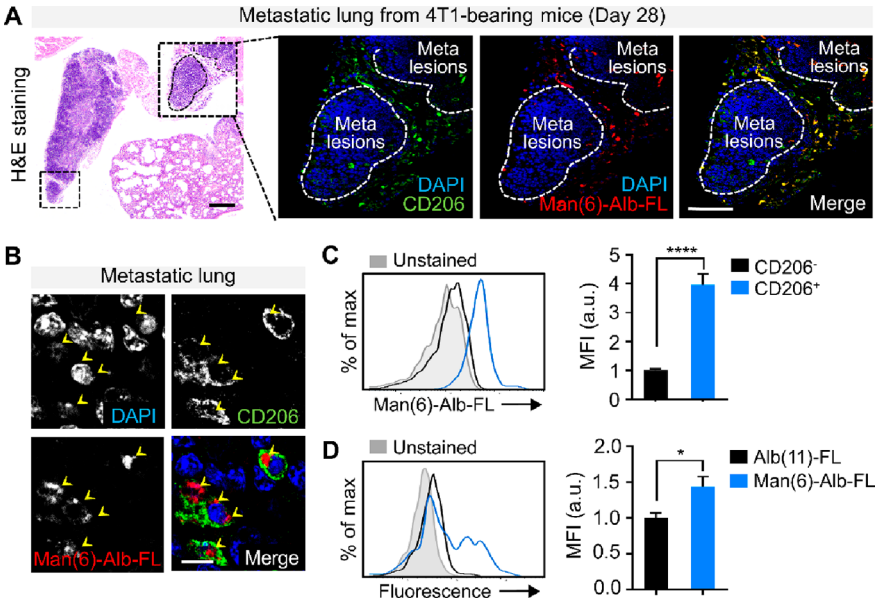

Figure 5. Confirmation of Man(6)-Alb-FL as a macrophage-targeted probe. (A) Representative H&E stained images of lungs from 4T1-bearing mice injected with Man(6)-Alb-FL 28 days after tumor injection (left). Representative confocal immunofluorescent images showing *in vivo* colocalization of injected Man(6)-Alb-FL (red) with the CD206$^+$ macrophages (green) within the lungs from 4T1-bearing mice, as confirmed in the overlay image (yellow). The white dotted lines indicate metastatic nodules in the lung. Scale bar = 75 μm. Higher magnification view (B) further demonstrates CD206$^+$ macrophage-specific uptake (yellow arrowheads) *in vivo*. DAPI, blue. Scale bar = 10 μm. (C,D) Quantification of CD206$^+$ macrophage-specific uptake *in vivo* using flow cytometry. (C) Man(6)-Alb-FL uptake by each gated CD206$^-$ macrophage (CD45$^+$CD11b$^+$F4/80$^+$CD206$^-$) and CD206$^+$ macrophage (CD45$^+$CD11b$^+$F4/80$^+$CD206$^+$) subset was determined from the fold change in the mean fluorescence intensity (MFI) of colabeled fluorescent dye (FNR-648). (D) Fold change in MFI of colabeled FNR-648 on CD206$^+$ macrophages from 4T1-bearing mice following injection with Alb(11)-FL or Man(6)-Alb-FL. n = 4–7 mice/group. Data represent the mean ± SEM. *P < 0.05, ****P < 0.0001 using Student's t test.

expression in TN tissues was closely associated with metastasis-related clinicopathological indices such as tumor stage, lymph node metastasis, ductal cell *in situ* (DCIS), and vimentin, an epithelial-to-mesenchymal transition marker (Figure S14C and D).

Next, we performed a pilot analysis of a small number of resected tumor tissues from human breast cancer patients to investigate whether MSA could be used to visualize macrophages in these tissues. Fresh breast tumor tissues after resection surgery were incubated with Man(6)-Alb-FL for 2 h, followed by *ex vivo* fluorescence imaging to evaluate Man(6)-Alb-FL uptake in these tissues (Figure 7A). Consistent with observations obtained from CD206 staining of human breast cancer tissues (Figure S14), the uptake of Man(6)-Alb-FL was more evident in tumor tissues of patients with TN (n = 10) than in those with ER$^+$/PR$^+$ breast cancer (n = 12) (Figure 7B and C), and costaining with CD206 revealed that a large proportion of CD206$^+$ cells incorporated Man(6)-Alb-FL (Figure 7D). Further quantitative measurements of the fluorescence signals of Man(6)-Alb-FL revealed a positive correlation between the number of CD206$^+$ cells and their uptake (Figure 7E), indicating that MSA might be differentially incorporated by CD206$^+$ cells in human tissues. In addition, as expected, among the 22 tumor tissues obtained from each group, the Man(6)-Alb-FL signal intensity in TN tumor tissues was more than three times higher than that in ER$^+$/PR$^+$ tumor tissues (Figure 7F and G).

CONCLUSIONS

In this study, we sought to investigate the benefits of targeting cellular components enriched in metastatic niches, particularly macrophages, for noninvasive visualization of lung metastasis. Using a click reaction to functionalize albumin, we developed the macrophage-targeted probe, MSA, which is especially useful for *in vivo* lung imaging with an optimized blood circulation time by introducing six molecules of mannose (Man(6)-Alb). In lung metastasis models, whole-body imaging with optimized MSA can noninvasively monitor macrophage accumulation in the lungs of tumor-bearing mice upon tumor progression, even when the metastatic burden is low. Furthermore, the fluorescence imaging of patient tumor samples *ex vivo* has broadened its potential clinical applicability. When translated to clinical settings, the ease of preparation and cost-effectiveness of MSA can be considerably advantageous for its use as a metastasis screening method for high-risk patients. Thus, MSA could be a promising monitoring tool that can provide additional information regarding the degree of metastatic disease, which is instructive for the early diagnosis of metastasis and therapeutic interventions.

METHODS

General. All reagents were purchased from Sigma-Aldrich (St. Louis, MO, USA), unless otherwise stated. Azadibenzocyclooctyne-*N*-hydroxysuccinimide (ADIBO-NHS), 2,2′,2″-(2-(4-(3-(3-azidopropyl)thioureido)benzyl)-1,4,7-triazonane-1,4,7-triyl)triacetic acid (NOTA-N_3), and azido-Flamma 648 (FNR646-N_3) were purchased from FutureChem (Seoul, Korea). 1-*O*-(2-(2-(2-Azidoethoxy)ethoxy)ethoxy)-α-D-mannopyranoside (Man-N_3) was purchased from Iris Biotech GmbH (Marktredwitz, Germany). HSA was purchased from MP Biomedicals (Aurora, OH, USA). Distearoylphosphatidylcholine (DSPC), cholesterol, istearoylphosphatidylethanolamine (DSPE), and DBCO-PEG2000-DSPE were purchased from Avanti Polar Lipids Inc. (Alabaster, AL, USA). Instant thin-layer chromatography-silica gel (ITLC-SG) plates were pur-

https://doi.org/10.1021/acsnano.2c03075
ACS Nano XXXX, XXX, XXX−XXX

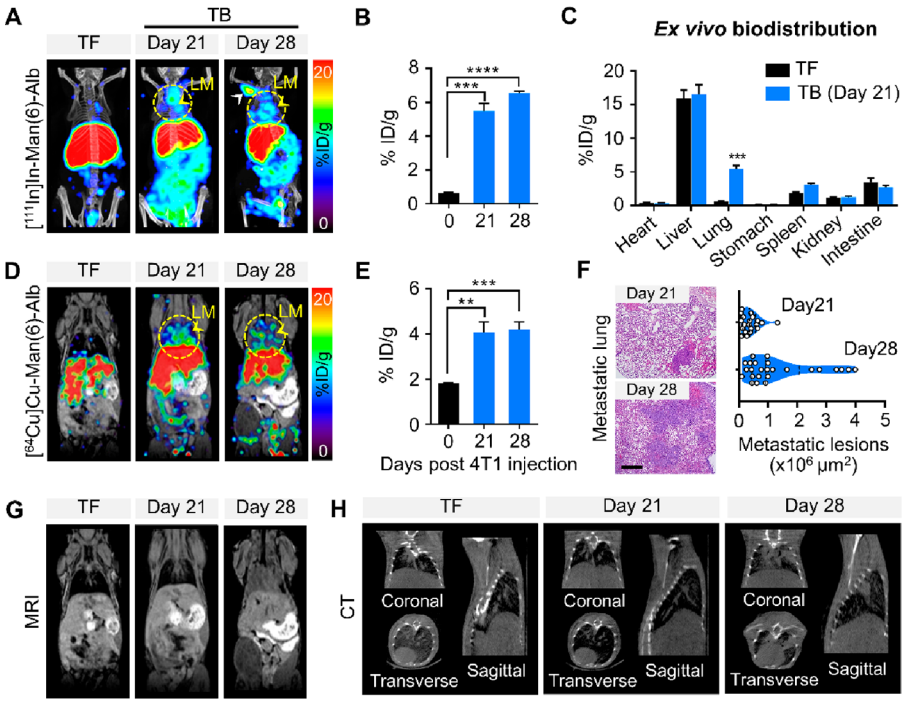

Figure 6. Multimodal imaging of Man(6)-Alb-FL in lung metastasis models. (A) Representative SPECT/CT images (MIP) with [^{111}In]In-Man(6)-Alb-FL in tumor-free (TF) and 4T1-bearing mice (TB) on days 21 and 28. The images revealed that [^{111}In]In-Man(6)-Alb-FL was able to detect lung metastases (LM, yellow arrowheads) at an earlier time (day 21) when metastatic burden was relatively low. A strong signal was also observed in the lymph node (white arrowhead). (B) Quantification of [^{111}In]In-Man(6)-Alb-FL signal in the resected lung, expressed as % ID/g. (C) *Ex vivo* biodistribution of [^{111}In]In-Man(6)-Alb-FL in various organs of 4T1-bearing mice 21 days after tumor injection. (D−H) Simultaneous PET/MRI imaging of [^{64}Cu]Cu-Man(6)-Alb-FL and CT imaging were performed in tumor-free (TF) and 4T1-bearing mice (TB) on days 21 and 28. (D) Representative PET/MRI images of [^{64}Cu]Cu-Man(6)-Alb-FL. (E) Quantification of [^{64}Cu]Cu-Man(6)-Alb-FL signal in the resected lung, expressed as % ID/g. (F) Representative H&E stained images and quantification of metastatic lesion area in lungs from 4T1-bearing mice on days 21 and 28. Scale bar = 50 μm. (G,H) MRI (G) and CT (H) images (coronal, transverse, and sagittal views) are also shown. Representative MRI and CT images show strong signals from lung metastases on day 28, while no significant change was detected at an earlier stage (day 21). n = 5−10 mice/group. Data represent mean ± SEM. **P < 0.01, ***P < 0.001, ****P < 0.0001 using Student's t test.

chased from Agilent Technologies, Inc. (Santa Clara, CA, USA). The PD-10 desalting columns were obtained from GE Healthcare (Buckinghamshire, UK). Radioactivity was measured using a gamma scintillation counter (Packard Cobra II; GMI, NM, USA). The molecular weights of HSA and its conjugates were determined using MALDI-TOF/TOF mass spectrometry with the TOF/TOF 5800 system (AB Sciex, Foster City, CA, USA). The hydrodynamic diameter and size distribution of the nanoparticles were analyzed using a DLS system and/or nanoparticle tracking analysis (Zetasizer Nano ZS90 and/or NanoSight, Malvern Instruments Ltd., Worcestershire, UK). The albumin concentration was spectrophotometrically measured using a NanoDrop ND-1000 spectrophotometer (NanoDrop Technologies, Wilmington, DE, USA).

Cells. Primary macrophages were differentiated from the mouse bone marrow cells. Bone marrow cells were obtained from 7−12 week old C57BL/6J male mice and differentiated into mature bone marrow-derived macrophages (BMDMs) for 7 days in Roswell Park Memorial Institute (RPMI)-1640 media containing 10% fetal bovine serum (FBS), 1% penicillin/streptomycin (PS), and 2 mM L-glutamine (Gibco), supplemented with recombinant murine GM-CSF (25 ng/mL, Miltenyi Biotec) for GM-BMMs or murine M-CSF (50 ng/mL, Miltenyi Biotec) for M-BMMs. The medium was replaced on days 3 and 5 with fresh medium containing GM-CSF or M-CSF. The breast carcinoma cell line, 4T1, melanoma cell line, B16F10, and LLC cell line were cultured in RPMI-1640 medium supplemented with 10% FBS and 1% PS. All cells were cultured at 37 °C in a humidified incubator containing 5% CO_2.

Synthesis of MSA Derivatives. A schematic diagram showing the synthesis of MSA derivatives is shown in Figures 1A and S1A. MSA derivatives were synthesized using a previous method with slight modifications.[31] Briefly, albumin (20 mg, 294 nmol) in phosphate buffered saline (PBS, pH 7.4, 0.5 mL) was reacted with 3.5, 7, 14, and 28 equiv of ADIBO-NHS in 2% dimethyl sulfoxide. The mixture was stirred at room temperature for 2 h and purified using a desalting column (PD-10) with PBS as an eluent to obtain 38 mg/mL ADIBO-albumin (AD-Alb, 280 nmol).

For fluorescence labeling, ADIBO-albumin (280 nmol) was reacted with N_3-FNR648 (28 nmol) for 30 min. After the reaction, AD-Alb-fluorescence (AD-Alb-FL) was purified and concentrated using a centrifugal filter. It is noteworthy that all the Alb-FL described later contain FL with the same number of conjugations. Man-N_3 was mixed with quantified Alb-FL for conjugation of ADIBO and N_3 groups using a click reaction to produce different numbers of mannosylated Alb-FL (Man-Alb-FL). Finally, radiolabeled NOTA-N_3 ([^{111}In]In-NOTA-N_3 or [^{64}Cu]Cu-NOTA-N_3) was conjugated with Alb-FL or Man-Alb-FL via a click reaction to generate radiolabeled-MSA ([^{111}In]In-Man-Alb-FL, [^{64}Cu]Cu-Man-Alb-FL, RI-Man-Alb-FL, or RI-Alb-FL), respectively. The ADIBO incorporation (DOF) and concentration of albumin were also determined using an UV−visible spectrophotometer (NanoDrop, Thermo Fisher) and calculations using MALDI-TOF data. Briefly, the molar concentration of albumin and ADIBO from AD-Alb was calculated using A280 (UV absorbance of ADIBO-albumin at 280 nm), A309 (UV absorbance of ADIBO-albumin at 309 nm), and the specific epsilons of albumin and ADIBO based on the Beer−Lambert law. This method indicates that the DOF of AD-Alb can be estimated rapidly and easily using only UV−vis analysis without performing MALDI-TOF. The 4 and 6 molar excesses of Man-N_3 were mixed with AD-Alb-FL that contained 6

https://doi.org/10.1021/acsnano.2c03075
ACS Nano XXXX, XXX, XXX−XXX

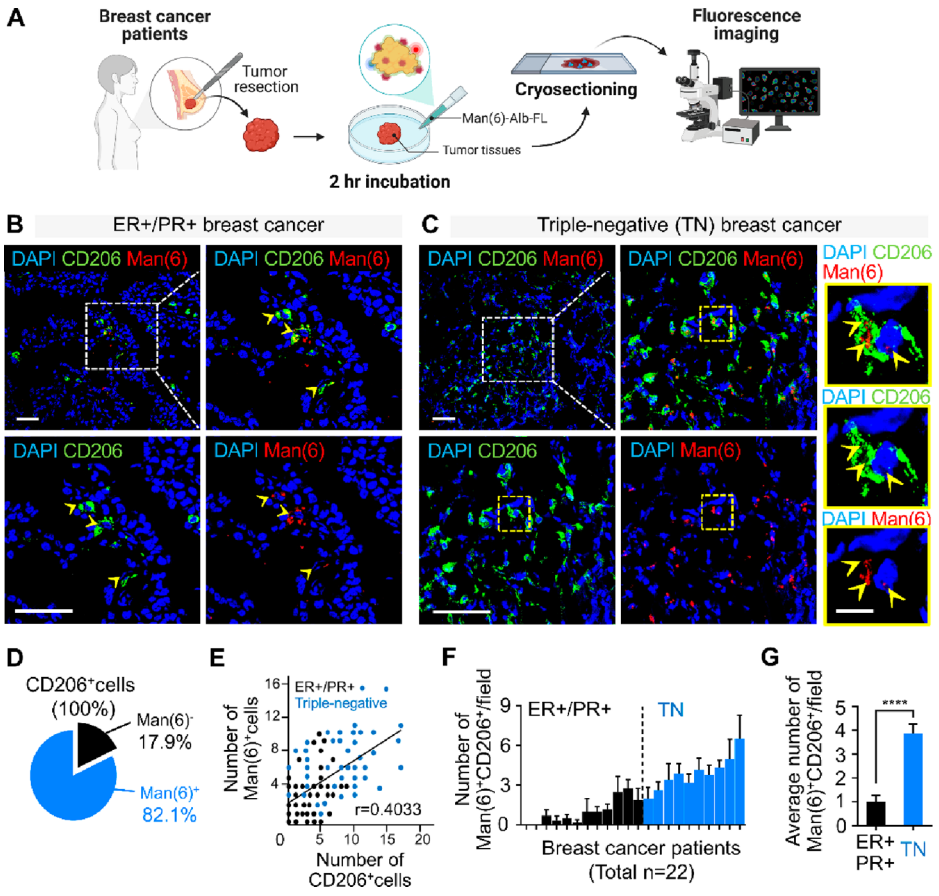

Figure 7. Fluorescence imaging of human breast cancer tissues with Man(6)-Alb-FL. (A) Illustration of fluorescence imaging of Man(6)-Alb-FL in resected tumor tissues from breast cancer patients. (B,C) Representative confocal immunofluorescent images of CD206 (green), Man(6)-Alb-FL (red), and DAPI (nucleus, blue) in ER^+/PR^+ (n = 12) (B) and triple-negative (TN) (n = 10) (B) human breast tumor sections 2 h after Man(6)-Alb-FL administration. Yellow arrowheads indicate Man(6)-Alb-FL-loaded $CD206^+$ cells (B). Higher magnification images of the yellow-outlined area also show Man(6)-Alb-FL uptake in $CD206^+$ cells (yellow arrowheads) in a triple-negative breast tumor section (C). Scale bar = 50 μm for images in (B) and (C), and 10 μm for the yellow magnified images in (C). (D) Pie chart indicating the percentage of Man(6)-Alb-FL uptake by $CD206^+$ cells in human breast tumor sections. (E) Correlation analysis of $CD206^+$ cells and Man(6)-Alb-FL-positive cells ($Man(6)^+$ cells) in human breast tumor sections. Black and blue dots indicate ER^+/PR^+ (n = 12) and triple-negative (TN) (n = 10) breast tumor sections, respectively. (F) The number of Man(6)-Alb-FL-positive ($Man(6)^+$) $CD206^+$ cells in ER^+/PR^+ (n = 12, black) and triple-negative (TN) (n = 10, blue) human breast tumor sections. (G) The average number of $Man(6)^+CD206^+$ cells in ER^+/PR^+ and TN human breast tumor sections. For quantification, 3−6 nonoverlapping images per section were counted. Data show means ± SEM. ****P < 0.0001 using Student's t-test.

DOF (AD-Alb(6)-FL), and the 8 and 12 molar excesses of Man-N_3 were mixed with CAN that contained 11 DOF (AD-Alb(11)-FL). The number of mannosyl groups on Man-Alb-FL was calculated using MALDI-TOF. This was also confirmed from the change in the absorbance value of ADIBO (A309) before and after the reaction of AD-Alb-FL with the azide-functionalized compounds.

Cell Viability Assay. M-BMMs were seeded in a 96-well plate at a density of 2 × 10^5 cells/mL in 100 μL of medium and incubated for 24 h for cell attachment. Various concentrations of Man(6)-Alb-FL were added to each well and incubated for 1 or 24 h at 37 °C. Then, 10 μL of Cell Counting Kit-8 (CCK-8, Dojindo) reagent was added and the cells were incubated for another 4 h at 37 °C in accordance with the manufacturer's instructions. Optical density of solutions was determined on a microplate reader (PerkinElmer, Waltham, MA, USA) at 450 nm.

Cellular Uptake of Man(6)-Alb-FL. To observe cellular uptake, GM-BMMs, M-BMMs, and 4T1 cells were incubated with 1 nmol of Man(6)-Alb-FL for 1 h at 37 °C. Cellular uptake of Man(6)-Alb-FL was determined by fluorescence imaging and flow cytometry. In mannan inhibition experiments, M-BMMs were preincubated at 37 °C for 20 min with 2 mg/mL mannan (Sigma, St. Louis, MO). Subsequently, 1 nmol of Man(6)-Alb-FL was added to the cells for 1 h at 37 °C and uptake was analyzed by flow cytometry.

Radiochemistry. The radioisotope-containing vial (370 MBq of ^{111}In or ^{64}Cu) was dried under N_2 flow in a lead-shielded fume hood for 20 min. After the vial was completely dried, 100 μL of 1 M sodium acetate buffer (pH 5.3) was added to the vial, followed by NOTA-N_3 (10 μg, 15 nmol) in distilled water (10 μL), and incubated at 70 °C for 10 min to obtain quantitative amounts of [^{111}In]In-NOTA-N_3 or [^{64}Cu]Cu-NOTA-N_3. Finally, 37 MBq (10 μL) of [^{111}In]In-NOTA-N_3 or [^{64}Cu]Cu-NOTA-N_3 was mixed with Alb-FL or Man-Alb-FL (500 μg, 73.5 nmol, 0.5 mL) in PBS and incubated at room temperature for 30 min to obtain quantitative yield of radiolabeled [^{111}In]In-Man-Alb-FL or [^{64}Cu]Cu-Man-Alb-FL.

The radiolabeling efficiency was determined using radio-instant thin layer chromatography-silica gel (radio-ITLC-SG) and a 0.1 M citric acid solution as the mobile phase. The R_f values of the free ^{111}In (or ^{64}Cu), [^{111}In]In-NOTA-N_3 (or [^{64}Cu]Cu-NOTA-N_3), and radiolabeled MSA were 0.9−1.0, 0.7−0.8, and 0.0−0.1, respectively (Figure S4). The stabilities of RI-Alb-FL and RI-Man-Alb-FL were assessed 24 h after labeling to confirm the stable conjugation of the radiolabeled agent during the imaging procedure (Figure S5).

https://doi.org/10.1021/acsnano.2c03075
ACS Nano XXXX, XXX, XXX−XXX

Study Approval. Animal experiments were performed in accordance with the Institute for Experimental Animals College of Medicine guidelines and the Guide for the Care and Use of Laboratory Animals prepared by the Institutional Animal Care and Use Committee of Seoul National University (accession number SNU-150708-1-1). Informed consent was obtained from each patient with the approval of the Institutional Review Board (C-1805-059-945).

Quantitative Real-Time Polymerase Chain Reaction. Total RNA was extracted using the TRIzol reagent (Invitrogen) according to the manufacturer's instructions. cDNA was synthesized from 1 μg of total RNA using reverse transcription, and the amount of mRNA was determined using real-time PCR analysis with the SYBR Green qPCR Pre-Mix (Enzynomics, Daejeon, South Korea) on an ABI real-time PCR 7500 machine (Applied Biosystems, CA, USA). Gene expression was normalized to housekeeping gene 18sRNA. Primer sequences were as follows: CD206 (forward: 5- AATGAAGATCAA-GCGCTGC-3; reverse: 5-TGACACCCAGCGGAATTTCT-3); and 18sRNA (forward: 5-GCAATTATTCCCCATGAACG-3; reverse: 5-GGCCTCACTAAACCATCCAA-3).

Immunofluorescence Staining. Cryostat sections (4 μm) were fixed in 4% paraformaldehyde (PFA), blocked, and permeabilized in blocking buffer (5% goat serum, 0.3% Triton X-100 in PBS) for 60 min at room temperature. For staining, the sections were incubated with the primary antibody against CD206 (1:200, Abcam) overnight at 4 °C and then with Alexa Fluor-conjugated secondary antibody (1:500, Alexa Fluor 488 goat antirabbit IgG (H+L), Invitrogen) for 2 h at room temperature. For fluorescence imaging with Man(6)-Alb-FL using fresh tumor tissues from breast cancer patients (n = 22), the freshly resected tumor tissues, without fixation, were rinsed with PBS and incubated with Man(6)-Alb-FL (20 μg/500 μL PBS) for 2 h, followed by CD206 staining. The accumulation of MSA within the tumor tissue was analyzed using confocal microscopy. The sections were counterstained with 1 mg/mL DAPI solution (Sigma-Aldrich). Images were acquired using a Leica TCS SP8 confocal fluorescence microscope.

Immunohistochemistry. Human breast tissue microarrays (TMAs) were constructed from archival tumor blocks (formalin-fixed, paraffin-embedded tissues) of breast cancer patients, including those with ER^+/PR^+ (294) and triple-negative breast cancer (396), after surgical intervention, at Seoul National University Hospital, from 1997 to 2003. The study was approved by the institutional review boards of the institutions of the collaborating pathologists and conducted in accordance with the Declaration of Helsinki. All patients participating in the study provided written informed consent. Clinicopathological information was obtained by reviewing pathology reports and from H&E-stained sections.

Immunohistochemistry was performed according to the manufacturer's instructions. Paraffin-embedded sections were deparaffinized, hydrated with Tris-buffered saline (TBS), and blocked with H_2O_2. For antigen retrieval, the slides were pretreated by steaming in sodium citrate buffer (10 mM sodium citrate, pH 6.0). After blocking in a blocking solution (10% FBS, 1% serum albumin in TBS), the slides were incubated overnight at 4 °C with rabbit anti-CD206 antibody (1:200, Abcam). The sections were washed three times in TBS with Tween-20, followed by incubation with biotinylated secondary polyclonal goat anti-rabbit antibodies (Dako, Glostrup, Denmark). Staining was performed using DAB chromogen solution (Dako) to allow proper development of brown color and counterstaining with hematoxylin. The slides were imaged using a digital camera (Leica DFC 290) at 100× magnification. The immunostaining was evaluated after blinding the clinicopathological information, and scoring was based on the number of CD206-positive cells, which were classified based on the intensity of immunostaining as negative, weak, moderate, and strong.

Flow Cytometry. The anti-mouse CD16/32 antibody (clone number 93) was added to single-cell suspensions from primary tumors and lungs to block nonspecific binding of immunoglobulin to macrophage Fc receptors, followed by staining with the following antibodies: anti-mouse CD45 (30-F11), CD11b (M1/70, BD Biosciences), and F4/80 (BM8). All antibodies were obtained from eBioscience, unless otherwise indicated. An additional antibody used for flow cytometry analysis included CD206 (Abcam), which was followed by staining with the appropriate secondary antibodies. Data were acquired using LSRFortessa (BD Bioscience) and analyzed using the FlowJo software (Tree Star).

PET Image Acquisition and Analysis of the Time−Activity Curve. PET images were acquired using preclinical PET/X-ray scanner (Sofie Bioscience) to confirm pharmacokinetic parameters and biodistribution of [^{64}Cu]Cu-Man-Alb-FL and [^{64}Cu]Cu-Alb-FL of varying mannosylation number. Simultaneously, the same amount of each derivative was added to mice, and all images were acquired for 5 min at 0, 2, 4, and 24 h after injection.

SPECT/CT Image Acquisition and Analysis. Animal SPECT/CT imaging was performed using a four-headed multipinhole NanoSPECT (Bioscan Inc., Washington DC) at 24 h after the intravenous injection of either [^{111}In]In-Man(6)-Alb-FL or [^{111}In]In-Alb(11)-FL. For quantitative analysis of the SPECT/CT image sequence, automatically programmed software in the GE workstation produced a volume of interest (VOI) of images, presented as mean counts.

Biodistribution Analysis. The biodistribution of [^{111}In]In-Man(6)-Alb-FL and [^{111}In]In-Alb(11)-FL was evaluated in 4T1-bearing mice. At 24 h after injecting [^{111}In]In-Man(6)-Alb-FL or [^{111}In]In-Alb(11)-FL, the animals were sacrificed and dissected for organ collection. Radioactivity in each organ was measured using a gamma counter. Counts per minute were decay-corrected, and the results were expressed as % ID/g.

Animal Models. For tumor models, syngeneic BALB/c mice for 4T1 cells and syngeneic C57BL/6 mice for B16F10 and LLC cells were used. Orthotopic tumor injections were performed by administering 4T1 cells (2×10^5) into the inguinal right fourth mammary fat pads of 7−8 week old female mice. At the end of the experiment, 4T1 tumor-bearing mice were injected with luciferin (PerkinElmer) and monitored using a Xenogen IVIS 200 imaging system (Xenogen, Alameda, CA, USA). For metastasis of lung carcinoma, LLC cells (3×10^5) were injected into the flank of 7−8 week old female mice. For intravenous injections, single-cell suspensions of 5×10^4 and 1×10^5 4T1 cells or 2×10^5 B16F10 cells in 100 μL PBS were injected into the tail vein. For blocking studies, Man(6)-Alb-FL was coinjected into mice with 100 μL mannan (25 mg/mL in Saline)

[^{64}Cu]Cu-Man-Alb-FL PET/MRI Image Acquisition and Analysis. All PET/MRI data used in this experiment were acquired using a simultaneous PET/MRI system (Aspect Imaging; Shoham, Israel). The SimPET system consists of a 1-T permanent magnet-based MRI and SiPM-based PET insert. The SimPET insert has a peak sensitivity of 3.4% and a center volumetric resolution of 0.53 mm^3. For imaging, 11.1 MBq was injected 1 h after injection, and simultaneous PET/MRI scans were performed for 5 min using a T1-weighted gradient echo (GRE) MR sequence (TR/TE, 25/3 ms; flip angle, 45°). PET/MRI images using [^{64}Cu]Cu-Man-Alb-FL were obtained at the same time point as SPECT/CT imaging of [^{111}In]In-Man-Alb-FL 24 h after intravenous injection.

The PET and MRI images were evaluated via visual inspection to detect any abnormal lesions indicative of metastatic nodules in the lungs. After quantitative analysis, spherical VOIs, 3 mm in diameter, were drawn over the MRI images of the lungs of each mouse. Uptake in the lung was estimated by applying VOIs (drawn on MRI images) over the respective simultaneously acquired PET images. The mean standard uptake value (SUV_{mean}) was calculated as follows:

$$SUV_{mean} = (\text{mean activity measured in the VOIs, Bq/mL}) / (\text{injected dose, Bq/body weight, g})$$

The PET images obtained using [^{64}Cu]Cu-Man-Alb-FL were analyzed using MIMvista (MIM Software Inc., USA). The three-dimensional region of interest was used for the quantitative evaluation of uptake in the lung, liver, and tumor (for the models).

https://doi.org/10.1021/acsnano.2c03075
ACS Nano XXXX, XXX, XXX−XXX

Statistical Analysis. All statistical analyses were performed using the GraphPad Prism software (version 6.0), and results are displayed as the mean ± standard error of the mean (SEM) or standard deviation (SD). A difference was considered to be significant at *P*-values less than 0.05, and differences are represented by $*P < 0.05$; $**P < 0.01$; $***P < 0.001$; and $****P < 0.0001$.

ASSOCIATED CONTENT

Supporting Information

The Supporting Information is available free of charge at https://pubs.acs.org/doi/10.1021/acsnano.2c03075.

Synthesis of RI-Man-Alb-FL; UV spectra and size of albumins; TEM images of AD-Alb(6), Man(2)-Alb, Man(4)-Alb, and Man(8)-Alb; labeling efficiency of all MSAs used in experiments; labeling stability of Alb(11)-FL and Man(6)-Alb-FL; *in vitro* CD206-specific uptake of Man(6)-Alb-FL in macrophages; *in vivo* PET imaging of [^{64}Cu]Cu-Man(6)-Alb-FL after treatment with mannan in tumor-free mice; *in vivo* SPECT/CT imaging of [^{111}In]In-Man(6)-Alb-FL after treatment with mannan in tumor-bearing mice; [^{111}In]In-Man(6)-Alb-FL noninvasively shows metastatic lesions in lungs in B16F10 melanoma-bearing mice; *ex vivo* biodistribution of [^{111}In]In-Alb(11)-FL and [^{111}In]In-Man(6)-Alb-FL 24 h after injection; CD206-specific uptake of [^{111}In]In-Man(6)-Alb-FL in primary tumor; *in vivo* [^{64}Cu]Cu-Man(6)-Alb-FL imaging of lung metastases in LLC tumor-bearing mice; *in vivo* PET imaging of [^{64}Cu]Cu-Man(6)-Alb-FL after treatment with mannan in 4T1 tumor-bearing mice; strong correlation between CD206 expression and metastatic potential in human breast tumor tissues (PDF)

AUTHOR INFORMATION

Corresponding Authors

Yun-Sang Lee − *Department of Biomedical Sciences, Seoul National University College of Medicine, Seoul 03080, Republic of Korea; Department of Nuclear Medicine, Seoul National University Hospital, Seoul 03080, Republic of Korea; Cancer Research Institute, Seoul National University, Seoul 03080, Republic of Korea*; Email: wonza43@snu.ac.kr

Seung Hyeok Seok − *Macrophage Lab, Department of Microbiology and Immunology, and Institute of Endemic Disease, Seoul National University College of Medicine, Seoul 03080, Republic of Korea; Department of Biomedical Sciences, Seoul National University College of Medicine, Seoul 03080, Republic of Korea*; orcid.org/0000-0002-4315-0688; Email: lamseok@snu.ac.kr

Authors

Hyewon Chung − *Macrophage Lab, Department of Microbiology and Immunology, and Institute of Endemic Disease, Seoul National University College of Medicine, Seoul 03080, Republic of Korea; Bio-MAX Institute, Seoul National University, Seoul 03080, Republic of Korea*

Ji Yong Park − *Department of Biomedical Sciences, Seoul National University College of Medicine, Seoul 03080, Republic of Korea; Department of Nuclear Medicine, Seoul National University Hospital, Seoul 03080, Republic of Korea; Cancer Research Institute and Dental Research Institute, Seoul National University, Seoul 03080, Republic of Korea*

Kyuwan Kim − *Department of Nuclear Medicine, Seoul National University Hospital, Seoul 03080, Republic of Korea; Cancer Research Institute, Seoul National University, Seoul 03080, Republic of Korea*

Ran Ji Yoo − *Department of Nuclear Medicine, Seoul National University Hospital, Seoul 03080, Republic of Korea; Cancer Research Institute, Seoul National University, Seoul 03080, Republic of Korea*

Minseok Suh − *Department of Molecular Medicine and Biopharmaceutical Sciences, Graduate School of Convergence Science and Technology, Seoul National University, Seoul 03080, Republic of Korea*

Gyo Jeong Gu − *Macrophage Lab, Department of Microbiology and Immunology, and Institute of Endemic Disease, Seoul National University College of Medicine, Seoul 03080, Republic of Korea*; orcid.org/0000-0003-0521-4270

Jin Sil Kim − *Department of Nuclear Medicine, Seoul National University Hospital, Seoul 03080, Republic of Korea*

Tae Hyeon Choi − *Department of Nuclear Medicine, Seoul National University Hospital, Seoul 03080, Republic of Korea; Department of Molecular Medicine and Biopharmaceutical Sciences, Graduate School of Convergence Science and Technology, Seoul National University, Seoul 03080, Republic of Korea*

Jung Woo Byun − *Department of Nuclear Medicine, Seoul National University Hospital, Seoul 03080, Republic of Korea*

Young Wook Ju − *Department of Surgery and Cancer Research Institute, Seoul National University College of Medicine, Seoul 03080, Republic of Korea*

Wonshik Han − *Department of Surgery and Cancer Research Institute, Seoul National University College of Medicine, Seoul 03080, Republic of Korea*

Han Suk Ryu − *Department of Pathology, Seoul National University College of Medicine, Seoul 03080, Republic of Korea*

Gehoon Chung − *Dental Research Institute, Seoul National University, Seoul 03080, Republic of Korea; Department of Oral Physiology, Seoul National University, School of Dentistry, Seoul 03080, Republic of Korea*

Do Won Hwang − *Department of Nuclear Medicine, Seoul National University Hospital, Seoul 03080, Republic of Korea; Research and Development Center, THERABEST, Co. Ltd., Seoul 03080, Republic of Korea*

Yujin Kim − *Department of Biomedical Sciences, Seoul National University College of Medicine, Seoul 03080, Republic of Korea*

Hye-Ryun Kang − *Department of Biomedical Sciences, Seoul National University College of Medicine, Seoul 03080, Republic of Korea*

Yi Rang Na − *Transdisciplinary Department of Medicine and Advanced Technology, Seoul National University Hospital, Seoul 03080, Republic of Korea*

Hongyoon Choi − *Department of Nuclear Medicine, Seoul National University Hospital, Seoul 03080, Republic of Korea*

Hyung-Jun Im − *Department of Molecular Medicine and Biopharmaceutical Sciences, Graduate School of Convergence Science and Technology, Seoul National University, Seoul 03080, Republic of Korea; Research Institute for Convergence Science, Seoul National University, Seoul 08823, Republic of Korea*; orcid.org/0000-0002-4368-6685

https://doi.org/10.1021/acsnano.2c03075
ACS Nano XXXX, XXX, XXX−XXX

Complete contact information is available at:
https://pubs.acs.org/10.1021/acsnano.2c03075

Author Contributions

‡H. Chung and J. Y. Park contributed equally.

Notes

The authors declare no competing financial interest.

ACKNOWLEDGMENTS

We thank Massimiliano Mazzone (KU Leuven, VIB Center for Cancer Biology, Belgium) for providing the LLC cell line. This work was supported by Korean Heath Technology R&D Project, Ministry of Health and Welfare (HI19C0339), Korea Drug Development Fund funded by Ministry of Science and ICT, Ministry of Trade, Industry, and Energy, and Ministry of Health and Welfare (HN22C0644, Republic of Korea), Basic Science Research Program through the National Research Foundation of Korea (NRF) funded by the Ministry of Science & ICT (2020R1C1C1012963, 2020M3H1A1073304, 2020R1A2C2010202, and 2021R1A2C3009427).

REFERENCES

(1) Altorki, N. K.; Markowitz, G. J.; Gao, D.; Port, J. L.; Saxena, A.; Stiles, B.; McGraw, T.; Mittal, V. The lung microenvironment: an important regulator of tumour growth and metastasis. *Nature Reviews Cancer* **2019**, *19* (1), 9−31.

(2) Di Gioia, D.; Stieber, P.; Schmidt, G. P.; Nagel, D.; Heinemann, V.; Baur-Melnyk, A. Early detection of metastatic disease in asymptomatic breast cancer patients with whole-body imaging and defined tumour marker increase. *Br. J. Cancer* **2015**, *112* (5), 809−18.

(3) O'Connor, J. P.; Aboagye, E. O.; Adams, J. E.; Aerts, H. J.; Barrington, S. F.; Beer, A. J.; Boellaard, R.; Bohndiek, S. E.; Brady, M.; Brown, G.; Buckley, D. L.; Chenevert, T. L.; Clarke, L. P.; Collette, S.; Cook, G. J.; deSouza, N. M.; Dickson, J. C.; Dive, C.; Evelhoch, J. L.; Faivre-Finn, C.; Gallagher, F. A.; Gilbert, F. J.; Gillies, R. J.; Goh, V.; Griffiths, J. R.; Groves, A. M.; Halligan, S.; Harris, A. L.; Hawkes, D. J.; Hoekstra, O. S.; Huang, E. P.; Hutton, B. F.; Jackson, E. F.; Jayson, G. C.; Jones, A.; Koh, D. M.; Lacombe, D.; Lambin, P.; Lassau, N.; Leach, M. O.; Lee, T. Y.; Leen, E. L.; Lewis, J. S.; Liu, Y.; Lythgoe, M. F.; Manoharan, P.; Maxwell, R. J.; Miles, K. A.; Morgan, B.; Morris, S.; Ng, T.; Padhani, A. R.; Parker, G. J.; Partridge, M.; Pathak, A. P.; Peet, A. C.; Punwani, S.; Reynolds, A. R.; Robinson, S. P.; Shankar, L. K.; Sharma, R. A.; Soloviev, D.; Stroobants, S.; Sullivan, D. C.; Taylor, S. A.; Tofts, P. S.; Tozer, G. M.; van Herk, M.; Walker-Samuel, S.; Wason, J.; Williams, K. J.; Workman, P.; Yankeelov, T. E.; Brindle, K. M.; McShane, L. M.; Jackson, A.; Waterton, J. C. Imaging biomarker roadmap for cancer studies. *Nat. Rev. Clin Oncol* **2017**, *14* (3), 169−186.

(4) Di Gioia, D.; Stieber, P.; Schmidt, G.; Nagel, D.; Heinemann, V.; Baur-Melnyk, A. Early detection of metastatic disease in asymptomatic breast cancer patients with whole-body imaging and defined tumour marker increase. *British journal of cancer* **2015**, *112* (5), 809−818.

(5) Weissleder, R.; Nahrendorf, M. Advancing biomedical imaging. *Proc. Natl. Acad. Sci. U. S. A.* **2015**, *112* (47), 14424−8.

(6) Daldrup-Link, H. E.; Golovko, D.; Ruffell, B.; Denardo, D. G.; Castaneda, R.; Ansari, C.; Rao, J.; Tikhomirov, G. A.; Wendland, M. F.; Corot, C.; Coussens, L. M. MRI of tumor-associated macrophages with clinically applicable iron oxide nanoparticles. *Clinical cancer research: an official journal of the American Association for Cancer Research* **2011**, *17* (17), 5695−704.

(7) Schroeder, A.; Heller, D. A.; Winslow, M. M.; Dahlman, J. E.; Pratt, G. W.; Langer, R.; Jacks, T.; Anderson, D. G. Treating metastatic cancer with nanotechnology. *Nature Reviews Cancer* **2012**, *12* (1), 39−50.

(8) Steeg, P. S. Targeting metastasis. *Nature reviews cancer* **2016**, *16* (4), 201−218.

(9) Zhang, K.; Wu, J.; Zhao, X.; Qin, J.; Xue, Y.; Zheng, W.; Wang, L.; Wang, H.; Shen, H.; Niu, T.; et al. Prussian Blue/Calcium Peroxide Nanocomposites-Mediated Tumor Cell Iron Mineralization for Treatment of Experimental Lung Adenocarcinoma. *ACS Nano* **2021**, *15* (12), 19838−19852.

(10) Perry, J. L.; Tian, S.; Sengottuvel, N.; Harrison, E. B.; Gorentla, B. K.; Kapadia, C. H.; Cheng, N.; Luft, J. C.; Ting, J. P.-Y.; DeSimone, J. M.; et al. Pulmonary delivery of nanoparticle-bound toll-like receptor 9 agonist for the treatment of metastatic lung cancer. *ACS Nano* **2020**, *14* (6), 7200−7215.

(11) Kitamura, T.; Qian, B.-Z.; Pollard, J. W. Immune cell promotion of metastasis. *Nature Reviews Immunology* **2015**, *15* (2), 73−86.

(12) Qian, B.-Z.; Pollard, J. W. Macrophage diversity enhances tumor progression and metastasis. *Cell* **2010**, *141* (1), 39−51.

(13) Wang, H.-F.; Liu, Y.; Yang, G.; Zhao, C.-X. Macrophage-mediated cancer drug delivery. *Materials Today Sustainability* **2021**, *11*, 100055.

(14) Lee, S. H.; Park, O. K.; Kim, J.; Shin, K.; Pack, C. G.; Kim, K.; Ko, G.; Lee, N.; Kwon, S.-H.; Hyeon, T. Deep tumor penetration of drug-loaded nanoparticles by click reaction-assisted immune cell targeting strategy. *J. Am. Chem. Soc.* **2019**, *141* (35), 13829−13840.

(15) Cao, H.; Dan, Z.; He, X.; Zhang, Z.; Yu, H.; Yin, Q.; Li, Y. Liposomes coated with isolated macrophage membrane can target lung metastasis of breast cancer. *ACS Nano* **2016**, *10* (8), 7738−7748.

(16) Choi, J.; Kim, H.-Y.; Ju, E. J.; Jung, J.; Park, J.; Chung, H.-K.; Lee, J. S.; Lee, J. S.; Park, H. J.; Song, S. Y.; et al. Use of macrophages to deliver therapeutic and imaging contrast agents to tumors. *Biomaterials* **2012**, *33* (16), 4195−4203.

(17) Wang, X.; Luo, G.; Zhang, K.; Cao, J.; Huang, C.; Jiang, T.; Liu, B.; Su, L.; Qiu, Z. Hypoxic tumor-derived exosomal miR-301a mediates M2 macrophage polarization via PTEN/PI3Kγ to promote pancreatic cancer metastasis. *Cancer research* **2018**, *78* (16), 4586−4598.

(18) Zhang, H.; Yu, Y.; Zhou, L.; Ma, J.; Tang, K.; Xu, P.; Ji, T.; Liang, X.; Lv, J.; Dong, W.; et al. Circulating tumor microparticles promote lung metastasis by reprogramming inflammatory and mechanical niches via a macrophage-dependent pathway. *Cancer Immunol. Res.* **2018**, *6* (9), 1046−1056.

(19) Locke, L. W.; Mayo, M. W.; Yoo, A. D.; Williams, M. B.; Berr, S. S. PET imaging of tumor associated macrophages using mannose coated 64Cu liposomes. *Biomaterials* **2012**, *33* (31), 7785−7793.

(20) Movahedi, K.; Schoonooghe, S.; Laoui, D.; Houbracken, I.; Waelput, W.; Breckpot, K.; Bouwens, L.; Lahoutte, T.; De Baetselier, P.; Raes, G.; et al. Nanobody-based targeting of the macrophage mannose receptor for effective in vivo imaging of tumor-associated macrophages. *Cancer Res.* **2012**, *72* (16), 4165−4177.

(21) Scodeller, P.; Simón-Gracia, L.; Kopanchuk, S.; Tobi, A.; Kilk, K.; Säälik, P.; Kurm, K.; Squadrito, M. L.; Kotamraju, V. R.; Rinken, A.; et al. Precision targeting of tumor macrophages with a CD206 binding peptide. *Sci. Rep.* **2017**, *7* (1), 14655.

(22) Li, Y.; Wu, H.; Ji, B.; Qian, W.; Xia, S.; Wang, L.; Xu, Y.; Chen, J.; Yang, L.; Mao, H. Targeted Imaging of CD206 expressing tumor-associated M2-like macrophages using mannose-conjugated anti-biofouling magnetic iron oxide nanoparticles. *ACS applied bio materials* **2020**, *3* (7), 4335−4347.

(23) Daldrup-Link, H. E.; Golovko, D.; Ruffell, B.; DeNardo, D. G.; Castaneda, R.; Ansari, C.; Rao, J.; Tikhomirov, G. A.; Wendland, M. F.; Corot, C.; et al. MRI of tumor-associated macrophages with clinically applicable iron oxide nanoparticles. *Clin. Cancer Res.* **2011**, *17* (17), 5695−5704.

(24) Sun, X.; Gao, D.; Gao, L.; Zhang, C.; Yu, X.; Jia, B.; Wang, F.; Liu, Z. Molecular imaging of tumor-infiltrating macrophages in a preclinical mouse model of breast cancer. *Theranostics* **2015**, *5* (6), 597.

(25) Zhang, C.; Yu, X.; Gao, L.; Zhao, Y.; Lai, J.; Lu, D.; Bao, R.; Jia, B.; Zhong, L.; Wang, F.; et al. Noninvasive imaging of CD206-positive

https://doi.org/10.1021/acsnano.2c03075
ACS Nano XXXX, XXX, XXX−XXX

M2 macrophages as an early biomarker for post-chemotherapy tumor relapse and lymph node metastasis. *Theranostics* **2017**, *7* (17), 4276.
(26) Zhao, P.; Yin, W.; Wu, A.; Tang, Y.; Wang, J.; Pan, Z.; Lin, T.; Zhang, M.; Chen, B.; Duan, Y.; et al. Dual-Targeting to Cancer Cells and M2Macrophages via Biomimetic Delivery of Mannosylated Albumin Nanoparticles for Drug-Resistant Cancer Therapy. *Adv. Funct. Mater.* **2017**, *27* (44), 1700403.
(27) Karimi, M.; Bahrami, S.; Ravari, S. B.; Zangabad, P. S.; Mirshekari, H.; Bozorgomid, M.; Shahreza, S.; Sori, M.; Hamblin, M. R. Albumin nanostructures as advanced drug delivery systems. *Expert opinion on drug delivery* **2016**, *13* (11), 1609−1623.
(28) Liu, Z.; Chen, X. Simple bioconjugate chemistry serves great clinical advances: albumin as a versatile platform for diagnosis and precision therapy. *Chem. Soc. Rev.* **2016**, *45* (5), 1432−1456.
(29) Maeda, H.; Seymour, L. W.; Miyamoto, Y. Conjugates of anticancer agents and polymers: advantages of macromolecular therapeutics in vivo. *Bioconjugate Chem.* **1992**, *3* (5), 351−362.
(30) Carter, D. C.; He, X. M.; Munson, S. H.; Twigg, P. D.; Gernert, K. M.; Broom, M. B.; Miller, T. Y. Three-dimensional structure of human serum albumin. *Science* **1989**, *244* (4909), 1195−8.
(31) Park, J. Y.; Song, M. G.; Kim, W. H.; Kim, K. W.; Lodhi, N. A.; Choi, J. Y.; Kim, Y. J.; Kim, J. Y.; Chung, H.; Oh, C.; et al. Versatile and finely tuned albumin nanoplatform based on click chemistry. *Theranostics* **2019**, *9* (12), 3398.
(32) Park, C. R.; Jo, J. H.; Song, M. G.; Park, J. Y.; Kim, Y.-H.; Youn, H.; Paek, S. H.; Chung, J.-K.; Jeong, J. M.; Lee, Y.-S.; et al. Secreted protein acidic and rich in cysteine mediates active targeting of human serum albumin in U87MG xenograft mouse models. *Theranostics* **2019**, *9* (24), 7447.
(33) Hirata, K.; Maruyama, T.; Watanabe, H.; Maeda, H.; Nakajou, K.; Iwao, Y.; Ishima, Y.; Katsumi, H.; Hashida, M.; Otagiri, M. Genetically engineered mannosylated-human serum albumin as a versatile carrier for liver-selective therapeutics. *Journal of controlled release* **2010**, *145* (1), 9−16.

https://doi.org/10.1021/acsnano.2c03075
ACS Nano XXXX, XXX, XXX−XXX